

# Tailoring the Fabrication Method of Dion–Jacobson 2D Halide Perovskites toward Highly Crystalline and Oriented Films

Zhengxun Lai, Zixin Zeng, You Meng, Yuxuan Zhang, Yi Shen, Wei Wang, Dengji Li, Dong Chen, Di Yin, Sai-Wing Tsang, SenPo Yip, and Johnny C. Ho\*

Halide perovskites are potential next-generation optoelectronic devices. However, the film quality of this charming material fabricated by the conventional spin-coating method is far from satisfactory, significantly affecting the optoelectronic devices' performance. Here, one facile slow-evaporating solvent (SE) method is demonstrated to synthesize high-quality organic–inorganic halide perovskite films. Compared with the conventional spin coating method, the films fabricated by this SE method show much higher crystallinity, oriented lattice, smoother surface morphology, and lower trap density. Besides, the photodetector manufactured by the SE method-based film also performs much better than the ones by the spin-coating method. Importantly, this universal method can be applied to different organic–inorganic halide perovskites, such as Dion–Jacobson (DJ) type and Ruddlesden–Popper type 2D halide perovskites and conventional 3D halide perovskites. This work gives an effective solution to improve the quality of the DJ-type halide perovskites, which endows the halide perovskites with a more practical chance to be commercialized cosmically.

commercialized on a large scale due to their poor stability, which is exactly the main challenge of this charming material.<sup>[5–7]</sup> Dimensionality reduction is one of the most effective methods to improve halide perovskites' performance and stability (ABX<sub>3</sub>; A = Cs, methylammonium or formamidine; B = Pb or Sn; and X = halogen).<sup>[8,9]</sup> For the 2D Ruddlesden–Popper (RP) halide perovskites (L<sub>2</sub>A<sub>n-1</sub>B<sub>n</sub>X<sub>3n+1</sub>; L is a long-chain monoamine), although the stability is enhanced to some extent comparable to the 3D counterparts, the weak van der Waals interactions among these 2D perovskites still make their performance not satisfactory in ambient environments.<sup>[10]</sup> Fortunately, the Dion–Jacobson type (DJ) of 2D halide perovskites (RA<sub>n-1</sub>B<sub>n</sub>X<sub>3n+1</sub>; R is a diamine) compensates for the weakness of the RP type. In contrast to the RP-type perovskites, the long-chain spacer cations in the DJ type are diamines without any van der Waals interactions. Accordingly,

## 1. Introduction

The power conversion efficiency of halide perovskite solar cells has been increasing dramatically and even approaching that of silicon solar cells just in several years since they were proposed.<sup>[1–4]</sup> However, the halide perovskites still cannot be

the DJ-type perovskites show superior stability to the RP type.<sup>[11–14]</sup> Ahmad et al. reported that the DJ-type halide perovskites with 1,3-propanediamine as the spacer cations were much more stable than the RP-type.<sup>[15]</sup> Zhao et al. introduced three new conjugated diamine spacer cations to the DJ-type 2D perovskites, which showed enhanced stability.<sup>[16]</sup> However, although DJ-type perovskites are much more stable and even have higher optoelectronic performance than RP-type, it is also a big challenge to fabricate high-quality DJ films through the conventional spin-coating method, where both the crystallinity and lattice orientation of the films are far from satisfactory. Wu et al. used methylammonium thiocyanate as an additive to get DJ-type perovskite films with preferred orientation and greater crystallinity.<sup>[17]</sup> Also, Zhang et al. used methylammonium chloride as an additive to reduce the trap-state densities in the films.<sup>[18]</sup> Solvent engineering has also been implemented to decrease trap-state density.<sup>[19]</sup> All these improvements were based on the spin-coating method, which can make the fabrication more cumbersome. In this regard, a facile fabrication method is urgently needed to give one perfect solution to the DJ-type perovskite's poor film quality.

In this work, we developed one facile slow-evaporation (SE) method to fabricate high-quality organic–inorganic DJ-type 2D

Z. Lai, Z. Zeng, Y. Meng, Y. Zhang, Y. Shen, W. Wang, D. Li, D. Chen, D. Yin, S.-W. Tsang, J. C. Ho  
Department of Materials Science and Engineering  
City University of Hong Kong  
Kowloon, Hong Kong SAR 999077, China  
E-mail: johnnyho@cityu.edu.hk

Y. Meng, J. C. Ho  
State Key Laboratory of Terahertz and Millimeter Waves  
City University of Hong Kong  
Kowloon, Hong Kong SAR 999077, China  
S. Yip, J. C. Ho  
Institute for Materials Chemistry and Engineering  
Kyushu University  
Fukuoka 816–8580, Japan

The ORCID identification number(s) for the author(s) of this article can be found under <https://doi.org/10.1002/adfm.202305539>

DOI: 10.1002/adfm.202305539

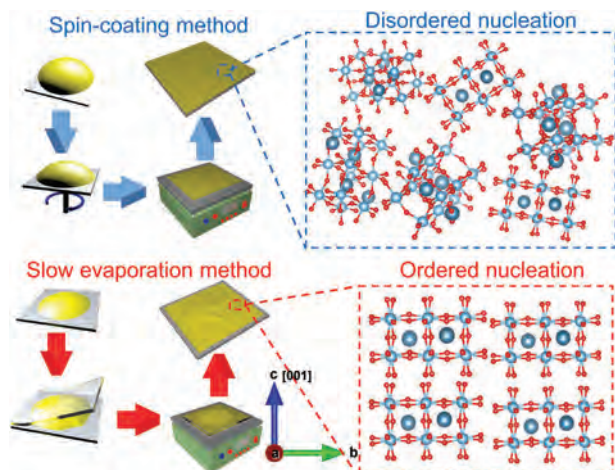


**Figure 1.** Schematics of the slow-evaporating solvent and conventional spin-coating methods.

halide perovskite films, which overcame the weakness of the conventional spin-coating method. The DJ-type films synthesized by this method showed higher crystallinity and preferred ordered lattice orientation, which benefits the transport of charge carriers for optoelectronic devices. Besides, the surface morphology of the fabricated films was also improved here. Then, the photodetection properties of the DJ-type perovskites fabricated by this SE method and the conventional spin-coating method were studied and compared in detail, which confirmed the enhanced performance attributable to the high film quality. Furthermore, we have also demonstrated that this universal method can also be applied to RP-type 2D halide perovskites and conventional 3D halide perovskites, yielding high-quality films. This work gives an effective method to fabricate high-quality DJ-type perovskite films, which can provide a clear research direction to acquire high-performance stable halide perovskite-based optoelectronic devices.

## 2. Results and Discussion

As depicted in **Figure 1**, the SE method in this work is demonstrated and compared with the conventional spin-coating (SC) method. For the SC method, the solvent evaporates immediately during the spin process, leading to poor crystallinity and film quality. For the SE method, however, the solvent will gradually permeate into the polydimethylsiloxane (PDMS) film first and evaporate slowly (for details of the method, see the Experimental Section). The long evaporating and annealing time provides a perfect environment for the ions and molecules to diffuse a longer distance in the film, which promotes the growth of the grains and yields much better crystallinity and film quality. Importantly, it is also known that the crystal orientation of the halide perovskites can be influenced by the nucleation environment in the solution. If the perovskite crystals nucleate from the air-liquid interface, then they will have preferential orientation.<sup>[20]</sup> For the conventional SC method, the perovskite crystallizes rapidly during the spin and annealing processes, making it random orientations. For the SE method, nevertheless, the crystals will nucleate at the air-liquid interface gradually, contributing to the

preferential-orientation growth. In addition, a large amount of solution (from tens to hundreds of microliters) is needed in the SC method to get a continuous and high-coverage film. However, most of the precursor solution is swung off and wasted during the spin process. But only several microliters of the solution are enough for the SE method, which is eco-friendly and beneficial to large-scale industrial production. Importantly, the film thickness fabricated by this SE method can be effectively controlled by changing the concentrations of the precursor solutions. As shown in Figure S1, Supporting Information, the DJ-type 2D perovskite films (DMPDAPbI<sub>4</sub>, DMPDA = *N,N*-dimethyl-1,3-propanediamine) with a thickness from tens of nanometers to two micrometers can be synthesized with different concentrations of the precursor solutions.

To demonstrate the feasibility of the advantages of this universal method, DMPDA-based DJ-type 2D perovskite films with halide ions of I<sup>-</sup> and Br<sup>-</sup> were studied, which are described as DMPDAI and DMPDABr here. **Figure 2a,b** shows the X-ray diffraction (XRD) results of the DMPDAI and DMPDABr films fabricated by both the SE and SC methods (DMPDAI-SE, DMPDAI-SC, DMPDABr-SE, and DMPDABr-SC) and the corresponding simulated XRD curves, respectively. To present the XRD details of the DMPDAI-SC and the DMPDABr-SC films, their enlarged views are also shown in Figures S2 and S3, Supporting Information. For both samples, one can see the XRD intensities of the films fabricated by the SE method are much larger than those fabricated by the conventional SC method, indicating the higher crystallinity of the former one. Besides, contrasting to the SC method, only the peaks of the (00*n*) planes of the films fabricated by the SE method appear, indicating the highly oriented growth of the films along [001] direction. In addition, for DMPDAI fabricated by the SE method, the full-width at half-maximum (FWHM) of the peak located at 8.66° ((001) plane) is as low as 0.09°, which is much lower than that fabricated by the conventional SC method (0.17°) (see Figure S4, Supporting Information). This observation suggests that the SE method can increase the grain size of the film largely. As we all know, the long-chain spacers in the 2D halide perovskite film can deter the transport of photo-generated carriers, leading to poor optoelectronic performance.<sup>[21]</sup> Since the long-chain spacer layers and inorganic layers are stacked along [001] direction in the film fabricated by the SE method, the photo-generated carriers can transfer freely through the inorganic framework (Figure 2c). However, due to the small grain sizes and their disordered orientation in the film fabricated by the conventional SC method, the photocurrent will be suppressed by the existence of organic spacers, impeding the collection of the photo-generated carriers (Figure 2d). These results imply that the larger grain size and highly-oriented lattice in the 2D halide perovskite films fabricated by the SE method can greatly enhance their optoelectronic performance. To further investigate the lattice information of the films, 2D grazing incidence X-ray diffraction (2D-GIXD) was also performed on the DMPDAI samples, which is more sensitive to the lattice orientation of thin films. As shown in Figure 2e, the Bragg spots of (001) plane of the DMPDAI-SE film with high intensity is obviously located at the *q<sub>z</sub>* direction, confirming the (001) plane is mainly stacked along the out-of-plane direction of the film. However, for the DMPDAI-SC film in Figure 2f, the Debye-Scherrer rings of different

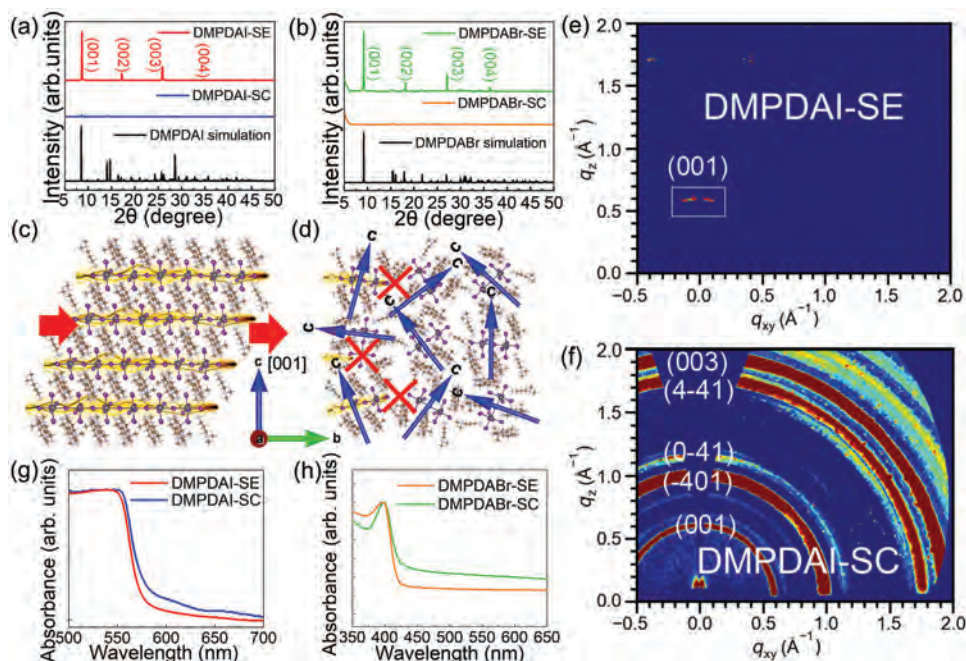


**Figure 2.** a,b) XRD and the corresponding simulation results of the DMPDAI and DMPDABr films fabricated by SE and SC methods. c,d) Schematics of the carriers transfer in the DJ-type halide perovskites films fabricated by the SE and SC methods, respectively. e,f) 2D-GIXD patterns for the DMPDAI-SE and DMPDAI-SC films. g,h) Absorption spectra of the DMPDAI and DMPDABr films fabricated by SE and SC methods.

planes are exhibited, which proves the totally random-oriented grains in the film. The 2D-GIXD results further confirm the highly-oriented lattice of the DMPDAI-SE film. In addition, the UV-vis absorption of the films was also measured and shown in Figure 2g,h. Only one sharp and pronounced absorption edge appears in all the films, indicating the pure-phase 2D perovskites. The corresponding Tauc plot is also demonstrated in Figure S5, Supporting Information, where the band gaps of the DMPDAI and DMPDABr films were determined to be around 2.22 and 3.00 eV, accordingly. Besides, we know that for the 2D materials, the unique quantum-well architecture commonly leads to optical anisotropy, which causes the absorbance parallel to the inorganic layers and spacer stacks to be larger than that perpendicular to them. We can see in Figure 2g,h, the optical absorption intensity of the films fabricated by the SE method is a little lower than those fabricated by the SC method, which corresponds to our conclusion above that the SE films are highly oriented with spacer layers and inorganic layers stacked along the out-of-plane direction.

To further investigate the quality of the DJ-type halide perovskite films, their morphology was then characterized by scanning electron microscopy (SEM) and atomic force microscopy (AFM). One can see in Figure 3a,b for the DMPDAI-SE film, the grain size is much larger than that of the DMPDAI-SC film, corresponding to the XRD results. Meanwhile, the root-mean-square (RMS) roughness of the DMPDAI-SE film is as low as 5.5 nm, which is also superior to that of the DMPDAI-SC one (72.1 nm), indicating a much smoother surface. Also, as depicted in the SEM images in Figure 3d,h, there are apparent pin-holes and islands-like grains on the DMPDABr-SC film. But the DMPDABr-SE film is dense and continuous (Figure 3c,g), suggesting it has a much higher quality than the DMPDABr-

SC one. The corresponding AFM images as well show the much smoother surface of DMPDABr-SE film (RMS = 16 nm) than that of DMPDABr-SC film (RMS = 108 nm). The SEM and AFM results again prove that the SE method can significantly improve the quality of the 2D halide perovskite films.

These films were then configured into photodetectors to assess the optoelectronic performance (see Experimental Section for details), where the device structure is shown in Figure S6, Supporting Information. A laser with a wavelength of 450 nm was used as the light source in the measurement of the DMPDAI samples. The current-voltage ( $I$ - $V$ ) curves of the DMPDAI samples under the illumination of the laser with different light intensities are shown in Figure S7, Supporting Information. The linear relationship suggests the near-ohmic contact between the electrodes and the DJ-type perovskite films, which benefits the photo-generated carriers' collection. The dark current of the DMPDAI-SE sample is as low as  $3 \times 10^{-12}$  A (Figure S7b, Supporting Information). As the light intensity increases to  $900 \text{ mW cm}^{-2}$ , the current immediately increases to  $1 \times 10^{-7}$  A with the on/off ratio as large as more than four orders of magnitude. Besides, the dark current of the DMPDAI-SC sample is found to be  $4 \times 10^{-13}$  A (Figure S7d, Supporting Information), which is even smaller than that of the DMPDAI-SE one. It is because the disordered lattice orientations and poor film quality block the transfer of the carriers. The dynamic photoresponse of the DMPDAI samples was also characterized by the current-time ( $I$ - $t$ ) measurement under an on-off switching laser with a light intensity of  $704 \text{ mW cm}^{-2}$  and a bias voltage of 1.5 V, which is shown in Figure 4a. Both photodetectors show stable and reversible photoswitching characteristics. Besides, the photocurrent of the DMPDAI-SE sample is more than seven times larger

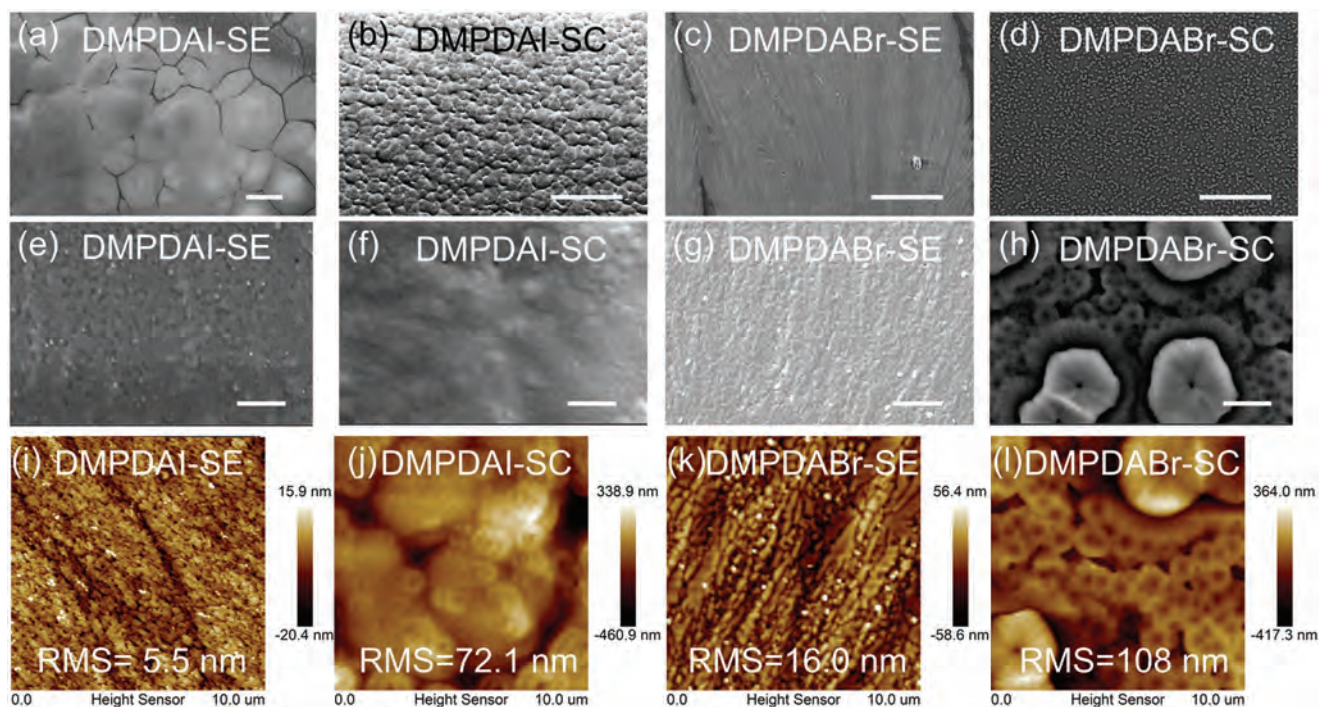


**Figure 3.** a–h) SEM images of the DMPDAI and DMPDABr films fabricated by SE and SC methods, where the scale bars in (a–d) are 100  $\mu\text{m}$ , and the scale bars in (e–h) are 1  $\mu\text{m}$ . i–l) AFM images of the DMPDAI and DMPDABr films fabricated by SE and SC methods.

than that of the DMPDAI-SC one, benefiting from the much higher-quality film. The photocurrents under different light intensities are also presented in Figure 4b, which shows a typical linear relationship. Moreover, the responsivity ( $R$ ), detectivity ( $D^*$ ), and external quantum efficiency (EQE) are also crucial parameters for photodetectors, which can thoroughly demonstrate the photodetector's capability to detect light. These parameters can be determined from the following equations:  $R = I_p/\Phi S$ ,  $D^* = S^{1/2}/(2eI_d)^{1/2}$  and  $\text{EQE} = hcR/e\lambda$ , where  $I_p$  is the photocurrent,  $\Phi$  the light intensity,  $S$  is the photodetector's active area. Also,  $e$  is the electronic charge,  $I_d$  is the dark current,  $h$  is Planck's constant,  $c$  is the velocity of light, and  $\lambda$  is the wavelength of the laser.<sup>[22]</sup> Figure 4c–e shows the  $R$ ,  $D^*$ , and EQE of the DMPDAI samples as the function of light intensity. All these three parameters show a sublinear relationship to the light intensity, which is often witnessed in layered semiconductor-based photodetectors due to the electron-hole generation, trapping, and recombination in device channels.<sup>[23,24]</sup> Besides, the  $R$ ,  $D^*$ , and EQE values of the DMPDAI-SE film are as large as 893  $\text{mA W}^{-1}$ ,  $2.4 \times 10^{12}$  Jones, and 247%, respectively, which are much larger than those of the DMPDAI-SC film, attributable to the favored lattice orientation and better film quality. The rise and decay times of the DMPDAI-SE film-based photodetector were also measured with the light intensity of 900  $\text{mW cm}^{-2}$  and displayed in Figure 4f to evaluate its response speed. It is observed that both the rise and decay times (the current increasing from 10% to 90% and decreasing from 90% to 10% of the maximum) are less than 500  $\mu\text{s}$ , which is superior to most of the reported state-of-art photodetectors. The photodetection parameters of the DMPDAI-SE sample are also compared with state-of-the-art organic–inorganic hybrid halide perovskites in Table 1. The polycrystalline film-based photode-

tor's performance is comparable with or even better than the crystalline devices. In addition, the DMPDABr-based photodetectors were also studied, where a 405-nm laser was used as the light source. The  $I$ – $V$  curves of the DMPDABr-SE-based photodetector shown in Figure S8, Supporting Information indicate that the dark current is as low as  $2.9 \times 10^{-12}$  A, which is still larger than the DMPDABr-SC sample ( $7.2 \times 10^{-13}$  A) because of its better crystallinity. The  $I$ – $t$  curves in Figure 4g depict a high on-off ratio of  $1.3 \times 10^4$ . The photocurrent of the DMPDABr-SE sample is almost 60 times larger than that of the DMPDAI-SC sample. As shown in Figure 4h–k, the photocurrents,  $R$ ,  $D^*$ , and EQE of the DMPDABr samples are sublinear to the light intensity, which is commonly seen in 2D materials-based photodetectors. The maximum  $R$ ,  $D^*$ , and EQE values of the DMPDABr-SE sample are 141  $\text{mA W}^{-1}$ ,  $3.8 \times 10^{11}$ , and 43%, respectively, which are also much larger than those of the DMPDAI-SC film. Accordingly, the response speed of the DMPDABr-SE sample was also characterized and presented in Figure 4l, where the light intensity was set at 290  $\text{mW cm}^{-2}$ . The rise and decay times are as short as 407 and 426  $\mu\text{s}$ . However, one can see that the DMPDAI film performs better than the DMPDABr film, which is caused by the inherent properties of the materials. To demonstrate this phenomenon, we performed first-principles calculations on these two materials to obtain their absorption coefficients. The absorption coefficients are shown in Figure S9, Supporting Information. It is obvious that within the laser wavelength we used in this work (300–500 nm), the absorption coefficient of DMPDAI is larger than DMPDABr. These results reveal the much higher photodetection performance of the 2D perovskite films fabricated by this facile SE method than those fabricated by the conventional spin-coating method.

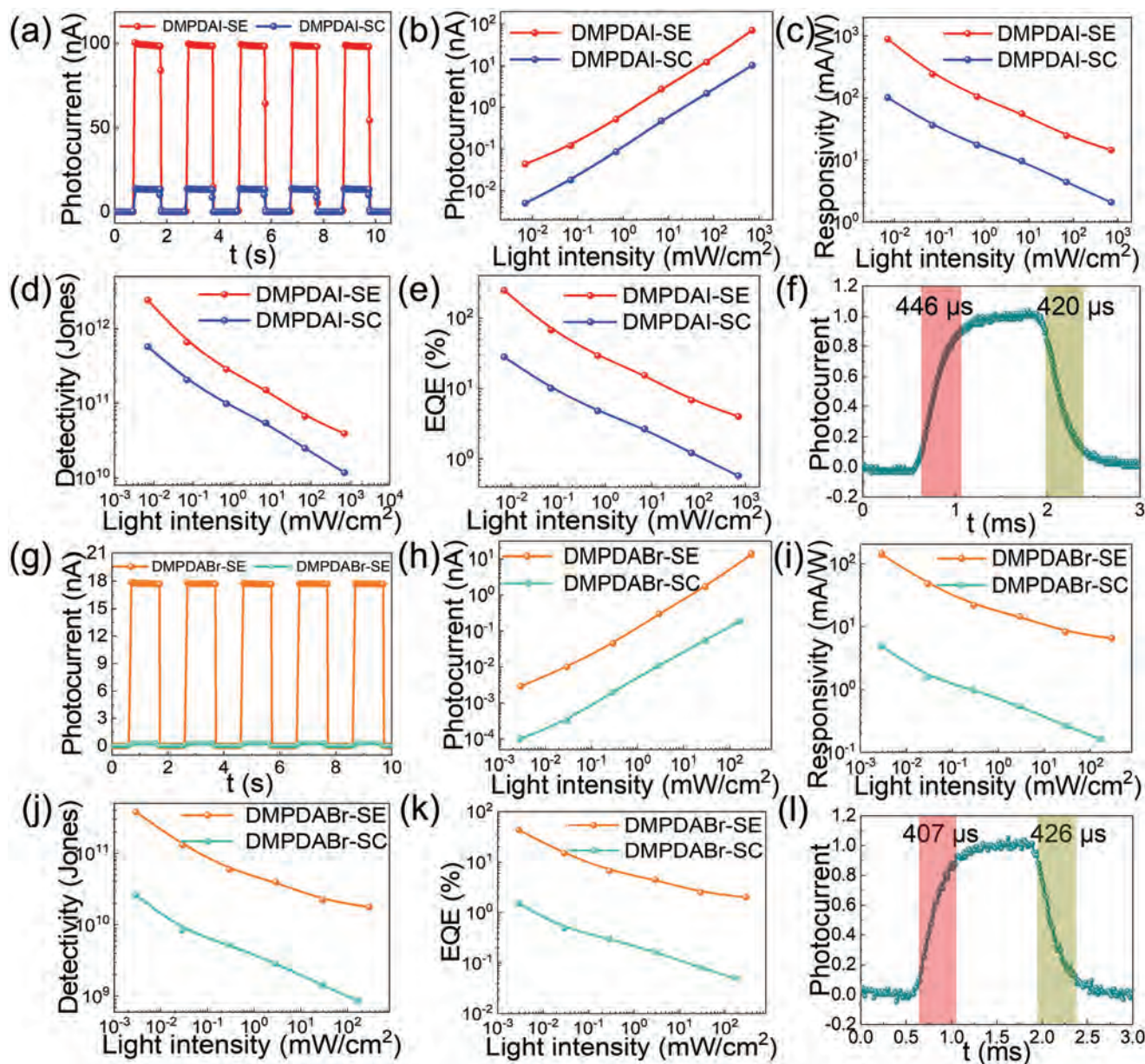


**Figure 4.** a) Time-dependent on-off switching of the DMPDAI samples fabricated by SE and SC methods. Dependence of b) photocurrent, c) responsivity, d) detectivity, e) EQE on the light intensity of the DMPDAI samples. f) High-resolution current versus time curve for the DMPDAI samples fabricated by SE method. g) Time-dependent on-off switching of the DMPDABr samples fabricated by SE and SC methods. Dependence of h) photocurrent, i) responsivity, j) detectivity, k) EQE on the light intensity of the DMPDABr samples. l) High-resolution current versus time curve for the DMPDABr sample fabricated by SE method.

Apart from the enhanced photoelectric properties, the stability of the perovskite films can also be promoted by the SE method. We all know that the halide perovskites are sensitive to light irradiation, which can lead to their decomposition.<sup>[25,26]</sup> Accordingly, the photoluminescence (PL) stability of the DMPDAI-SE and DMPDAI-SC films was studied. **Figure 5a** shows the PL spectra of these two films under the illumination of a 532 nm laser. The PL peaks are both located at about 550 nm, which corresponds to the absorption spectra in Figure 2. However, one can see the FWHM of the PL peak of DMPDAI-SE film is obviously

smaller than that of DMPDAI-SC film, confirming the better crystallinity of DMPDAI-SE film. The changes in the PL intensities of these two films under the continuous illumination of a high-intensity laser (about  $10^8 \text{ mW cm}^{-2}$ ) are shown in Figure 5b. The PL intensity of the DMPDAI-SC film decays rapidly to less than 20% of its initial value under the illumination of 30 s, suggesting that the perovskite film was decomposed. However, for the DMPDAI-SE film, the PL intensity can keep stable at a high value thanks to its good stability. Besides, we can see the PL intensity of the DMPDAI-SE film even increases a little at the

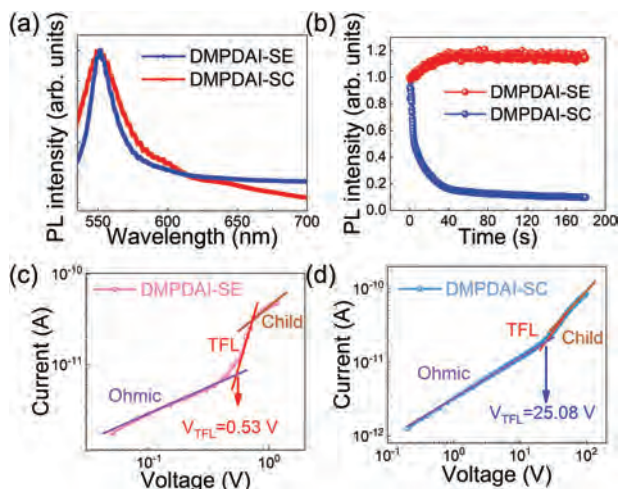


**Figure 5.** a) The PL spectra of the DMPDAI films fabricated by SE and SC methods. b) Change of the PL intensities of the peaks in (a) under continuous illumination of a 532-nm laser. c,d) Dark  $I$ - $V$  curves according to the SCLC model of the DMPDAI-SE and DMPDAI-SC films-based devices.

beginning, which can be caused by the defect curing by oxygen.<sup>[27]</sup> To further examine the quality of the films fabricated by the SE and SC methods, the trap densities of the films were also studied according to the space-charge-limited current (SCLC) model.<sup>[28,29]</sup> As shown in Figure 5c,d, as the bias voltage increases, ohmic, trap-filled limit (TFL), and Child's regions are clearly separated, and the onset voltage  $V_{TFL}$  is

**Table 1.** Comparison of various figure of merits of halide perovskites-based photodetectors.

Perovskites	On/off ratio	R [mA W <sup>-1</sup> ]	D* [Jones]	Rise/decay time [ms]	Reference
(C <sub>5</sub> H <sub>11</sub> NH <sub>3</sub> ) <sub>2</sub> (CH <sub>3</sub> NH <sub>3</sub> ) <sub>2</sub> Pb <sub>2</sub> I <sub>7</sub> crystal	>10 <sup>3</sup>	3.87	2.92 × 10 <sup>10</sup>	0.00152/0.00167	[37]
(PEA) <sub>2</sub> PbI <sub>4</sub> crystal	10.8	5	1.07 × 10 <sup>13</sup>	N/A	[38]
(iBA) <sub>2</sub> ((MA <sub>0.4</sub> FA <sub>0.6</sub> ) <sub>0.9</sub> CS <sub>0.1</sub> ) <sub>3</sub> Pb <sub>4</sub> I <sub>13</sub> film	720	400	1.68 × 10 <sup>12</sup>	43/22	[39]
(R)- $\alpha$ -(PEA) <sub>2</sub> PbI <sub>4</sub> crystal	124	600	3.06 × 10 <sup>11</sup>	22/34	[40]
(iso-BA) <sub>2</sub> PbI <sub>4</sub> crystal	10 <sup>3</sup>	560	1.23 × 10 <sup>10</sup>	233/166	[41]
(BA) <sub>2</sub> (MA) <sub>n-1</sub> PbnI <sub>3n+1</sub> flake	N/A	<30	5 × 10 <sup>8</sup>	10/10	[42]
MAPbI <sub>3</sub> nanowire	2.8 × 10 <sup>4</sup>	Tens	4.16 × 10 <sup>12</sup>	0.2/0.37	[43]
(BPA) <sub>2</sub> PbBr <sub>4</sub> crystal	10 <sup>4</sup>	0.1	10 <sup>7</sup>	0.027/0.03	[44]
(R)- $\beta$ [MPA] <sub>2</sub> MAPb <sub>2</sub> I <sub>7</sub> crystal	N/A	1100	2.3 × 10 <sup>11</sup>	3.5/4.9	[45]
PEAI treated (FAMAPb-(Br <sub>0.4</sub> I <sub>0.6</sub> ) <sub>3</sub> film	759	45.2	3.25 × 10 <sup>11</sup>	N/A	[8]
DMPDAPbI <sub>4</sub> film	3.3 × 10 <sup>4</sup>	893	2.4 × 10 <sup>12</sup>	0.446/0.420	This work

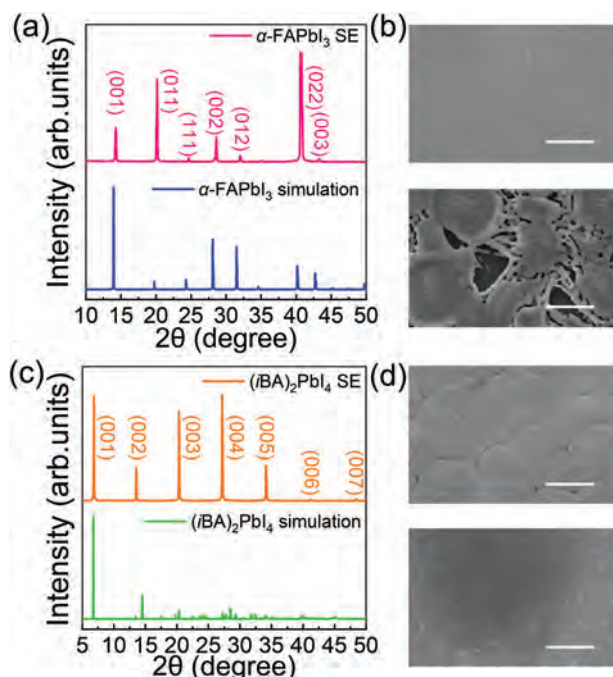


**Figure 6.** a) XRD pattern and the corresponding simulation result of the  $\alpha$  phase FAPbI<sub>3</sub> film fabricated by SE method. b) SEM images of the FAPbI<sub>3</sub> films fabricated by SE and SC methods, respectively, where the scale bars are 1  $\mu$ m. c) XRD pattern and the corresponding simulation result of (iBA)<sub>2</sub>PbI<sub>4</sub> film fabricated by SE method. d) SEM images of the (iBA)<sub>2</sub>PbI<sub>4</sub> films fabricated by SE and SC methods, respectively, where the scale bars are 1  $\mu$ m.

shown, which is related to the trap states ( $n_{\text{trap}}$ ) of the film:  $n_{\text{trap}} = 2\epsilon\epsilon_0 V_{TFL} / eL^2$ , where  $\epsilon$  is the relative dielectric constant (about 8.4, calculated by first-principles calculations),  $\epsilon_0$  is the vacuum permittivity, and  $L$  represents the length of the device channel.<sup>[30,31]</sup> Accordingly, for DMPDAI-SE film, a low trap density of  $4.9 \times 10^{10} \text{ cm}^{-3}$  is acquired, which is much lower than that of the DMPDAI-SC film ( $2.3 \times 10^{12} \text{ cm}^{-3}$ ), pointing to the much higher film quality of DMPDAI-SE sample.

Apart from the DJ-type 2D halide perovskites, this universal method can also be applied to other kinds of organic-inorganic halide perovskites. It needs to be pointed out that, for all-inorganic halide perovskites, one can use the SE method to fabricate microcrystals because of their poor solubility and good ability to crystallize.<sup>[32]</sup> For organic-inorganic halide perovskites, we found that high-quality 3D halide perovskite and RP-type 2D halide perovskite films can also be synthesized by the SE method. **Figure 6a** shows the XRD curve of the 3D halide perovskite FAPbI<sub>3</sub> (FA = formamidinium) film fabricated by the SE method, where it is suggested that pure  $\alpha$  phase FAPbI<sub>3</sub> was obtained. The absorption spectrum of the film is also shown in Figure S10, Supporting Information. The absorption edge is located at about 825 nm, confirming the black phase ( $\alpha$  phase) of the FAPbI<sub>3</sub> film. The SEM images of the FAPbI<sub>3</sub> films fabricated by the SE method and conventional SC methods are also shown in Figure 6b. Obviously, the coverage of the SC film is patchy, and the SE film is compact and smooth. It is because, for the SC method, the solvent volatilizes rapidly, leaving defects in the films. However,

for the SE method, the solvent can evaporate slowly, contributing to the homogeneous nucleation of the films. Figure 6c shows the XRD curve of the RP type 2D halide perovskite (*i*BA)<sub>2</sub>PbI<sub>4</sub> (*i*BA = iso-butylamine) film, where one can see only the peaks of the planes along [001] direction appear, indicating the highly oriented crystal lattice. Figure S11, Supporting Information, shows the absorption spectrum of the film, where the sharp absorption edge located at 542 nm further confirms its good crystallinity. Besides, the SEM image in Figure 6d of the (*i*BA)<sub>2</sub>PbI<sub>4</sub> film fabricated by the SE method also shows its large grain size. However, for the (*i*BA)<sub>2</sub>PbI<sub>4</sub> film fabricated by the SC method, there are obvious pin holes on the surface, confirming the superior quality of the SE-fabricating films. It needs to be pointed out that for DJ- and RP-type perovskites fabricated by the SE method, only <001> direction facets appear in the XRD results; however, for  $\alpha$ -FAPbI<sub>3</sub> film, <011> facets are dominant. It is because, as we have demonstrated before, the perovskite films fabricated by the SE methods have preferential orientation, but those fabricated by the conventional SC methods usually have random orientation. In this case, for the  $\alpha$ -FAPbI<sub>3</sub> films fabricated by the SC methods, <001> facets are usually dominant in the XRD results caused by the intrinsic higher XRD intensities of these facets.<sup>[33]</sup> But for the SE methods, the  $\alpha$ -FAPbI<sub>3</sub> film has a preferential orientation of <011> facets because of its lower enthalpy of formation.<sup>[34]</sup> However, the DJ- and RP-type 2D halide perovskite films fabricated by the SE methods have a preferential orientation of <001> direction due to the lower enthalpy of formation. At the same time, the intrinsic XRD intensities of these facets are also supposed to be dominant; hence, they only show <001> direction facets in XRD results.

### 3. Conclusion

In conclusion, one SE method was proposed to fabricate DJ-type halide perovskite films to overcome the fatal weakness of the conventional SC method. The films fabricated by this SE method show high crystallinity and highly ordered orientation, which can hardly be achieved by the conventional SC method but is urgently needed for optoelectronic devices. After being configured into photodetectors, it exhibited impressed photodetection performance with a high responsibility of 893 mA W<sup>-1</sup>, detectivity of 2.4 × 10<sup>12</sup> Jones, and fast response speed of less than 500  $\mu$ s, which is much superior to that of the conventional SC method. More importantly, this universal method can also be used to fabricate other kinds of organic–inorganic halide perovskites, including RP-type 2D halide perovskites and 3D halide perovskites. This work gives an alternative way to fabricate high-quality DJ-type 2D halide perovskites.

### 4. Experimental Section

**Synthesis of Materials:** The DJ-type perovskite DMPDAI (DMPDABr) precursor was prepared by dissolving DMPDAI<sub>2</sub> (DMPDABr<sub>2</sub>) and PbI<sub>2</sub> (PbBr<sub>2</sub>) at a molar ratio of 1:1 in dimethylformamide to form a 1 M solution. The RP-type perovskite precursor was prepared by dissolving *i*BAI and PbI<sub>2</sub> at a molar ratio of 2:1 in dimethylformamide to form a 1 M solution. 3D halide perovskite FAPbI<sub>3</sub> precursor was prepared by dissolving FAI and PbI<sub>2</sub> at a molar ratio of 1:1 in dimethylformamide to form a 1 M solution.

**Device Fabrication:** Glass substrates were ultrasonically cleaned using acetone, ethanol, and deionized water in succession. Then, these substrates were treated with a mild oxygen plasma to improve the hydrophilia. For the SE method, 4  $\mu$ L precursor solution was dripped on the substrate. After the spreading of the solution, a PDMS film was covered on the substrate, followed by thermal annealing at 60 °C for 2 h. For the conventional spin-coating method, 40  $\mu$ L precursor solution was spin-coated on the substrate at 3000 rpm for 30 s, followed by thermal annealing at 100 °C for 10 min. For the FAPbI<sub>3</sub> films, they were annealed at 190 °C for 5 min after the SE or SC method to get the  $\alpha$  phase. After that, with the assistance of shadow masks, 60-nm-thick symmetric Au electrodes were thermally evaporated onto the DJ-type halide perovskite films to configure photodetectors. The channel length and width of the photodetectors were 10 and 70  $\mu$ m, respectively.

**Film and Device Characterization:** The XRD patterns were acquired by D2 Phaser with Cu K $\alpha$  radiation, Bruker. The morphologies of the films were characterized using SEM (FEI Quanta 450 FEG SEM) and AFM (Bruker Dimension Icon AFM). The absorption spectra were recorded by Hitachi UH 4150 UV–vis absorption spectrophotometers. The PL spectra and the PL stability were studied by the Raman system (WITec RAMAN alpha 300R). For the 2D-GIXD measurement, films were radiated at 12.08 keV X-ray with an incident angle of 0.2°. The photodetection performance of the fabricated photodetectors was characterized by a standard electrical probe station and an Agilent 4155C semiconductor analyzer (Agilent Technologies, California, USA). Lasers with wavelengths of 450 and 405 nm were used as the light sources for the photodetector measurement, while the power of the incident irradiation was measured using a power meter (PM400, Thorlabs). An attenuator was also employed to tune the irradiation power illuminating the device. The schematic diagram of the experimental setup is depicted in Figure S12, Supporting Information. All the photodetection performance measurements were conducted in a light-tight environment to minimize external disturbance.

**Computational Details:** The first-principles calculations were performed using density functional theory as implemented in the Vienna Ab initio Simulation Package.<sup>[35]</sup> The model of the calculation is shown in Figure S13, Supporting Information. The generalized-gradient approximation for exchange–correlation energy proposed by Perdew, Burke, and Ernzerhof was used.<sup>[36]</sup> The convergence criteria for the energy and atomic forces were set to 5 × 10<sup>-4</sup> eV and 0.01 eV Å<sup>-1</sup>, respectively. The Brillouin zone was sampled with G-centered 5 × 5 × 5 *k* point meshes.

### Supporting Information

Supporting Information is available from the Wiley Online Library or from the author.

### Acknowledgements

The authors acknowledge the General Research Fund (CityU 11306520) of the Research Grants Council of Hong Kong SAR, China. S.-W.T. acknowledges the General Research Fund (CityU 11304420) from the Research Grants Council of Hong Kong SAR, China.

### Conflict of Interest

The authors declare no conflict of interest.

### Data Availability Statement

The data that support the findings of this study are available from the corresponding author upon reasonable request

### Keywords

crystalline, Dion–Jacobson, halide perovskites, photodetectors, oriented films

Received: May 18, 2023  
Revised: June 20, 2023  
Published online: July 19, 2023

- [1] Q. Jiang, J. Tong, Y. Xian, R. A. Kerner, S. P. Dunfield, C. Xiao, R. A. Scheidt, D. Kuciauskas, X. Wang, M. P. Hautzinger, R. Tirawat, M. C. Beard, D. P. Fenning, J. J. Berry, B. W. Larson, Y. Yan, K. Zhu, *Nature* **2022**, *611*, 278.
- [2] C. Wang, Y. Zhao, T. Ma, Y. An, R. He, J. Zhu, C. Chen, S. Ren, F. Fu, D. Zhao, X. Li, *Nat. Energy* **2022**, *7*, 744.
- [3] S. Wang, L. Tan, J. Zhou, M. Li, X. Zhao, H. Li, W. Tress, L. Ding, M. Graetzel, C. Yi, *Joule* **2022**, *6*, 1344.
- [4] NREL, Best Research-Cell Efficiency Chart, <https://www.nrel.gov/pv/cell-efficiency.html>. (accessed: January 2023).
- [5] K. Miyano, M. Yanagida, N. Tripathi, Y. Shirai, *J. Phys. Chem. Lett.* **2016**, *7*, 2240.
- [6] T. Leijtens, G. E. Eperon, N. K. Noel, S. N. Habisreutinger, A. Petrozza, H. J. Snaith, *Adv. Energy Mater.* **2015**, *5*, 1500963.
- [7] A. Aftab, M. I. Ahmad, *Sol. Energy* **2021**, *216*, 26.
- [8] T. Kim, S. Jeong, K. H. Kim, H. Shim, D. Kim, H. J. Kim, *ACS Appl. Mater. Interfaces* **2022**, *14*, 26004.
- [9] S. Sidhik, Y. Wang, M. De Siena, R. Asadpour, A. J. Torma, T. Terlier, K. Ho, W. Li, A. B. Puthirath, X. Shuai, A. Agrawal, B. Traore, M. Jones, R. Giridharagopal, P. M. Ajayan, J. Strzalka, D. S. Ginger, C. Katan, M. A. Alam, J. Even, M. G. Kanatzidis, A. D. Mohite, *Science* **2022**, *377*, 1425.
- [10] Z. Lai, R. Dong, Q. Zhu, Y. Meng, F. Wang, F. Li, X. Bu, X. Kang, H. Zhang, Q. Quan, W. Wang, F. Wang, S. Yip, J. C. Ho, *ACS Appl. Mater. Interfaces* **2020**, *12*, 39567.
- [11] J. Gong, M. Hao, Y. Zhang, M. Liu, Y. Zhou, *Angew. Chem., Int. Ed.* **2022**, *61*, e202112022.
- [12] Z. Lai, F. Wang, Y. Meng, X. Bu, X. Kang, Q. Quan, W. Wang, C. Liu, S. P. Yip, J. C. Ho, *Adv. Opt. Mater.* **2021**, *9*, 2101523.
- [13] M. Guan, Y. Xie, Y. Zhang, Z. Gu, L. Qiu, Z. He, B. Ye, A. Suwardi, Z. Dai, G. Li, G. Hu, *Adv. Mater.* **2023**, *35*, 2210611.
- [14] Y. Liu, H. Zhou, Y. Ni, J. Guo, R. Lu, C. Li, X. Guo, *Joule* **2023**, *7*, 1016.
- [15] S. Ahmad, P. Fu, S. Ahmad, P. Fu, S. Yu, Q. Yang, X. Liu, X. Wang, X. Wang, *Joule* **2018**, *3*, 794.
- [16] R. Zhao, R. P. Sabatini, T. Zhu, S. Wang, A. Morteza Najjarian, A. Johnston, A. J. Lough, S. Hoogland, E. H. Sargent, D. S. Seferos, *J. Am. Chem. Soc.* **2021**, *143*, 19901.
- [17] H. Wu, X. Lian, S. Tian, Y. Zhang, M. Qin, Y. Zhang, F. Wang, X. Lu, G. Wu, H. Chen, *Sol. RRL* **2020**, *4*, 2000087.
- [18] Y. Zhang, J. Wen, Z. Xu, D. Liu, T. Yang, T. Niu, T. Luo, J. Lu, J. Fang, X. Chang, S. Jin, K. Zhao, S. Liu, *Adv. Sci.* **2021**, *8*, 2001433.
- [19] D. Lu, G. Lv, Z. Xu, Y. Dong, X. Ji, Y. Liu, *J. Am. Chem. Soc.* **2020**, *142*, 11114.
- [20] A. Z. Chen, M. Shiu, J. H. Ma, M. R. Alpert, D. Zhang, B. J. Foley, D. M. Smilgies, S. H. Lee, J. J. Choi, *Nat. Commun.* **2018**, *9*, 4383.
- [21] J. Even, L. Pedesseau, C. Katan, *ChemPhysChem* **2014**, *15*, 3733.
- [22] Z. Lai, Y. Meng, F. Wang, X. Bu, W. Wang, P. Xie, W. Wang, C. Liu, S. P. Yip, J. C. Ho, *Nano Res.* **2022**, *15*, 3621.
- [23] C. Lan, R. Dong, Z. Zhou, L. Shu, D. Li, S. P. Yip, J. C. Ho, *Adv. Mater.* **2017**, *29*, 702759.
- [24] F. Binet, J. Y. Duboz, E. Rosencher, F. Scholz, V. Härle, *Appl. Phys. Lett.* **1996**, *69*, 1202.
- [25] Y. Deng, S. Xu, S. Chen, X. Xiao, J. Zhao, J. Huang, *Nat. Energy* **2021**, *6*, 633.
- [26] A. Coriolano, L. Polimeno, M. De Giorgi, F. Todisco, R. Mastria, V. Ardizzone, L. Dominici, D. Ballarini, A. Rizzo, G. Gigli, D. Sanvitto, L. De Marco, *Nanomaterials* **2021**, *11*, 465.
- [27] S. Chen, X. Wen, S. Huang, F. Huang, Y. Cheng, M. Green, A. Hobaillie, *Sol. RRL* **2017**, *1*, 1600001.
- [28] M. I. Saidaminov, A. L. Abdelhady, B. Murali, E. Alarousu, V. M. Burlakov, W. Peng, I. Dursun, L. Wang, Y. He, G. MacUlan, A. Goriely, T. Wu, O. F. Mohammed, O. M. Bakr, *Nat. Commun.* **2015**, *6*, 7586.
- [29] Z. Lai, F. Wang, Y. Meng, X. Bu, X. Kang, Q. Quan, W. Wang, S. Yip, C. Liu, J. C. Ho, *Sci. China Mater.* **2022**, *65*, 1313.
- [30] E. A. Duijnste, J. M. Ball, V. M. Le Corre, L. J. A. Koster, H. J. Snaith, J. Lim, *ACS Energy Lett.* **2020**, *5*, 376.
- [31] D. Shi, V. Adinolfi, R. Comin, M. Yuan, E. Alarousu, A. Buin, Y. Chen, S. Hoogland, A. Rothenberger, K. Katsiev, Y. Losovyj, X. Zhang, P. A. Dowben, O. F. Mohammed, E. H. Sargent, O. M. Bakr, *Science* **2015**, *347*, 519.
- [32] Z. Lai, Y. Meng, F. Wang, X. Bu, D. Chen, P. Xie, W. Wang, D. Li, Y. Zhang, W. Wang, C. Liu, S. P. Yip, J. C. Ho, *Adv. Opt. Mater.* **2022**, *10*, 2201127.
- [33] D. Wang, M. Chen, X. Zhang, L. Chao, T. Niu, Y. Lv, G. Xing, Y. Xia, M. Li, H. Zhang, Y. Chen, *ACS Appl. Mater. Interfaces* **2023**, *15*, 16818.
- [34] K. Shimamura, T. Hakamata, F. Shimojo, R. K. Kalia, A. Nakano, P. Vashishta, *J. Chem. Phys.* **2016**, *145*, 224503.
- [35] G. Kresse, J. Furthmüller, *Phys. Rev. B: Condens. Matter Mater. Phys.* **1996**, *54*, 11169.
- [36] J. P. Perdew, K. Burke, M. Ernzerhof, *Phys. Rev. Lett.* **1996**, *77*, 3865.
- [37] S. Han, P. Wang, J. Zhang, X. Liu, Z. Sun, X. Huang, L. Li, C. Ji, W. Zhang, B. Teng, W. Hu, M. Hong, J. Luo, *Laser Photonics Rev.* **2018**, *12*, 1800060.
- [38] C. H. Lin, B. Cheng, T. Y. Li, J. R. D. Retamal, T. C. Wei, H. C. Fu, X. Fang, J. H. He, *ACS Nano* **2019**, *13*, 1168.
- [39] R. Dong, C. Lan, F. Li, S. P. Yip, J. C. Ho, *Nanoscale Horiz.* **2019**, *4*, 1342.
- [40] J. Wang, C. Fang, J. Ma, S. Wang, L. Jin, W. Li, D. Li, *ACS Nano* **2019**, *13*, 9473.
- [41] L. Li, L. Jin, Y. Zhou, J. Li, J. Ma, S. Wang, W. Li, D. Li, *Adv. Opt. Mater.* **2019**, *7*, 1900988.
- [42] Q. Fu, X. Wang, F. Liu, Y. Dong, Z. Liu, S. Zheng, A. Chaturvedi, J. Zhou, P. Hu, Z. Zhu, F. Bo, Y. Long, Z. Liu, *Small* **2019**, *15*, 1902890.
- [43] D. Wu, H. Zhou, Z. Song, M. Zheng, R. Liu, X. Pan, H. Wan, J. Zhang, H. Wang, X. Li, H. Zeng, *ACS Nano* **2020**, *14*, 2777.
- [44] C. Ji, D. Dey, Y. Peng, X. Liu, L. Li, J. Luo, *Angew. Chem., Int. Ed.* **2020**, *59*, 18933.
- [45] L. Wang, Y. Xue, M. Cui, Y. Huang, H. Xu, C. Qin, J. Yang, H. Dai, M. Yuan, *Angew. Chem., Int. Ed.* **2020**, *59*, 6504.